

Multi-Winding Power Transformer Modeling for Fast-Front Transients

Nasirpour, F.; Luo, T.; Ghaffarian Niasar, M.; Popov, M.

10.1109/TPWRD.2025.3535419

Publication date

Document Version Final published version

Published in

IEEE Transactions on Power Delivery

Citation (APA)Nasirpour, F., Luo, T., Ghaffarian Niasar, M., & Popov, M. (2025). Multi-Winding Power Transformer Modeling for Fast-Front Transients. *IEEE Transactions on Power Delivery*, *40*(2), 1054-1066. https://doi.org/10.1109/TPWRD.2025.3535419

Important note

To cite this publication, please use the final published version (if applicable). Please check the document version above.

Other than for strictly personal use, it is not permitted to download, forward or distribute the text or part of it, without the consent of the author(s) and/or copyright holder(s), unless the work is under an open content license such as Creative Commons.

Takedown policy

Please contact us and provide details if you believe this document breaches copyrights. We will remove access to the work immediately and investigate your claim.

Green Open Access added to <u>TU Delft Institutional Repository</u> as part of the Taverne amendment.

More information about this copyright law amendment can be found at https://www.openaccess.nl.

Otherwise as indicated in the copyright section: the publisher is the copyright holder of this work and the author uses the Dutch legislation to make this work public.

Multi-Winding Power Transformer Modeling for Fast-Front Transients

Farzad Nasirpour, Tianming Luo, *Member, IEEE*, Mohamad Ghaffarian Niasar, *Member, IEEE*, and Marjan Popov, *Fellow, IEEE*

Abstract—This paper presents a comprehensive model for power transformers, by considering eddy current losses in both the core and conductors. This is achieved through a meticulous analytical approach that ensures high fidelity in representing the transformer's electromagnetic properties. The consideration of magnetic flux effects on inductance and resistance values significantly enhances the model's accuracy and validity. Traditional analytical methods often resort to simplified approaches due to the complexity of these calculations. The paper addresses these limitations by evaluating the eddy current losses in the core and conductors, and by providing a detailed understanding of each component's impact on transformer behavior. Furthermore, by considering the core and conductor effects on the magnetic field distribution, the model handles a wide range of frequencies, making it suitable for conducting comprehensive transient analysis. To validate the model, comparisons with the finite element method and empirical measurements are conducted. Additionally, a reduced-order transformer model is developed using admittance matrix reduction. This approach focuses on the nodes of interest, effectively eliminating not-observed nodes and reducing computational complexity without compromising accuracy. In this way, voltages at specific points of interest are computed efficiently, maintaining the accuracy of the original model.

Index Terms—Over-voltages, power system transients, power transformers, resonances, white-box modeling.

I. INTRODUCTION

OWER transformers are among the most vital and costly components in the power system. Their failure can cause severe consequences for the network, including prolonged interruption, high repair costs, and even potential hazards for the operators [1], [2]. In recent years, transient phenomena such as switching surges, voltage spikes, and line faults have accounted for 28% of transformer failures, with an additional 13% of failures attributed to lightning strikes [3]. Overvoltages and nonlinear voltage distribution originating from these phenomena

Received 16 July 2024; revised 19 November 2024; accepted 23 January 2025. Date of publication 28 January 2025; date of current version 20 March 2025. This research work was supported by the Nederlandse Organisatie voor Wetenschappelijk Onderzoek (NWO) in collaboration with TSO TenneT, DSO Alliander/Qirion, Royal Smit Transformers, and TSO National Grid, U.K., through the NWO-TTW Project "Protection of Future Power System Components (PRoteuS)" under Grant 18699. Paper no. TPWRD-01123-2024. (Corresponding author: Marjan Popov.)

The authors are with the Faculty of EEMCS, Delft University of Technology, 2628CD Delft, The Netherlands (e-mail: F.Nasirpour@tudelft.nl; T.Luo-1@tudelft.nl; M.Ghaffarianniasar@tudelft.nl; M.Popov@tudelft.nl).

Color versions of one or more figures in this article are available at https://doi.org/10.1109/TPWRD.2025.3535419.

Digital Object Identifier 10.1109/TPWRD.2025.3535419

can adversely affect the insulation parts of transformers [4]. As such, studying the behavior of transformers during these events is crucial for ensuring the reliable performance of the power grid. Given the impracticality of studying various power system configurations using real components, there is an urgent need for accurate transformer models capable of simulating electromagnetic transients [5], [6]. These models enable us to study the internal behavior of transformers and determine how transformers interact with other parts of the network, which can be crucial for various studies [5].

Transformer models can be classified as black, white, and grey-box models [5]. The white-box modeling approach is adopted to comprehensively examine the transformer's internal behavior and interactions with other parts of the network. Unlike black-box models, which primarily depend on external measurements and do not provide insight into the internal dynamics, the white-box model leverages the physical properties and structural parameters of the transformer. This approach allows us to study key phenomena, such as internal resonances within the windings, which are critical for understanding transformer performance from both terminal and internal perspectives. The accuracy of these models is determined by how well they represent the complex internal behaviors of transformers. In this regard, the finite element method (FEM) can be used to obtain the model parameters with reasonable accuracy [6], [7], [8]. FEM involves dividing the transformer into a large number of small, finite elements and solving the complex equations governing the electromagnetic field and material behavior within each element. While this approach can yield highly accurate results, it requires significant computational resources. Instead, this paper adopts an analytical approach, balancing accuracy with computational efficiency.

The transformer's broad frequency behavior is characterized by many resonant and anti-resonant frequencies resulting from windings' capacitances and inductances. When subjected to transient signals, these resonances may cause severe overvoltages inside the transformer. Therefore, identifying the main limiting factors in these scenarios is crucial for achieving more accurate simulation results. Despite extensive studies on high-frequency transformer modeling and behavior, such as those highlighted by CIGRE workgroup A2/C4.52 [9], there has yet to be a consensus on the effects of the losses in the core and conductors. Some researchers [10], claimed that the transformer core plays a significant role in damping transient overvoltages. They asserted that inductance values remain influential even at

0885-8977 © 2025 IEEE. All rights reserved, including rights for text and data mining, and training of artificial intelligence and similar technologies. Personal use is permitted, but republication/redistribution requires IEEE permission. See https://www.ieee.org/publications/rights/index.html for more information.

frequencies exceeding 1 MHz, contrary to the belief that the flux does not penetrate the core at very high frequencies. In [11], the authors concluded that for cases of open low-voltage winding, the laminated core becomes the primary source of losses in transformers. Additionally, authors in [12] demonstrated that the effective complex permeability of the power transformer core is substantial even at 1 MHz, asserting that eddy current losses in conductors are negligible compared to the core losses. The authors in [13] claimed that the magnetic core cannot be disregarded for frequencies above 10 kHz. Despite these findings, it is a common practice for high-frequency transformer modeling to treat transformers as air-core equipment, as indicated in [14], [15], [16], [17], [18]. This assumption indicates that conductor losses are the main limiting factor regarding the amplitude of overvoltages when the transformer is subjected to transient signals. In such conditions, conductor losses contribute to energy dissipation that reduces the peak overvoltages in the windings. This plays a crucial role in preventing excessive voltage stress on the transformer insulation, especially during fast-front transient events. Consequently, there is a need for accurate methods to consider and compare these effects in transformers and to find answers to yet-open questions.

On the other hand, the computation of losses in the conductors and core is a complex and challenging task. The intricate interactions of electromagnetic fields and material properties at various frequencies make accurate calculations difficult. Consequently, researchers often resort to simplified or empirical approaches to include these losses in their models [19], [20], [21]. While these methods may suffice for limited frequency ranges, their accuracy over a wide frequency range must be improved. It should be noted that eddy currents circulating in the conductive materials alter the magnetic flux distribution. This not only affects the losses in the model but also changes the inductance values with frequency, and affects the overall behavior of the transformer. The importance of this issue is also highlighted in CIGRE Joint Working Group A2/C4.52 [9] as quoted: "... given that the losses are strongly variable with frequency and that they are not susceptible to be represented with constant resistances, a model is required where the frequency variation of both the losses and the inductances are integrated, based on the behavior of eddy currents, thus obtaining a model with physical meaning".

Therefore, this paper aims to enhance the accuracy of whitebox analytical models and deepen our understanding of the phenomena occurring in transformers. To achieve this, frequencydependent winding losses and inductances are derived through precise analytical formulas. To this aim, the influence of the core-component flux (transformer core) and air-component flux on the values of inductances and resistances are considered separately. The effect of core-component flux is considered by replacing the transformer laminated core with a solid equivalent core that exhibits the same behavior and losses as the laminated one. This method is suitable for both analytical formula derivation and FEM computation. Unlike other methods, this approach does not require direct measurements on the transformer to obtain the necessary parameters, which simplifies the modeling procedure. To account for eddy current losses in conductors, a different set of equations is solved, allowing the separate study

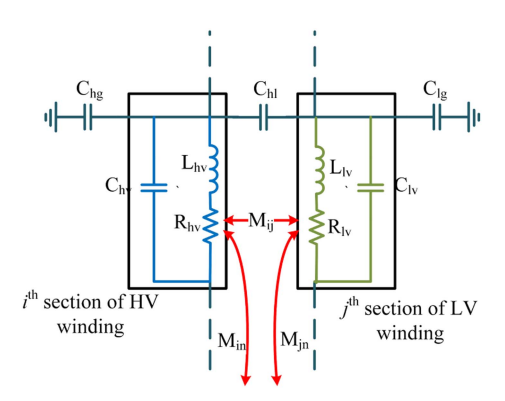


Fig. 1. An illustration of a transformer model.

of each damping mechanism. This can help resolve the ongoing debate about the relative importance of core and conductor losses. Besides, by considering both conductor and core losses and their effects on the inductance values, this paper significantly improves the accuracy of the detailed analytical models, making them suitable for studying a wide range of scenarios. Finally, to make the developed model suitable for system-level studies, a reduced-order model is developed and implemented in EMT-based software. This step makes sure that we do not lose any accuracy and information when obtaining a low-order model.

To demonstrate the model's performance, in this research, two power transformers with rated powers of 48 and 50 MVA, as well as an HV winding consisting of 22 disks, are investigated. The HV coil is designed to provide access to the terminals of each disk enabling voltage distribution measurements along the winding. General information about the transformers and the coil is provided in Appendix C. Please note that for the three-phase transformer, full access to the design data is restricted to the manufacturer due to confidentiality constraints.

The remainder of the paper is organized as follows. The procedures for determining the parameters and obtaining the full transformer model are presented in Sections II and III. Sections IV and V focus on model comparisons and validation based on measurements and EMT-based software implementation. Finally, the conclusions are elaborated in Section VI.

II. PARAMETER DETERMINATION

In the white box modeling approach, transformers can be modeled by lumped circuit elements that are inductances, resistances, and capacitances, or by distributed parameters using electromagnetic transmission line theory. In [22], it is shown that lumped-parameter models can provide sufficient accuracy for fast transient overvoltages. This method requires transformer windings to be subdivided into smaller sections. Then, each section can be represented by a circuit equivalent. A representation of this model can be seen in Fig. 1, where $L_{\rm hv},\,L_{\rm lv},\,M_{ij},\,M_{in},\,$ and $M_{\rm jn}$ represent the self-inductances of the HV and LV winding sections, the mutual impedance between them and between these sections and other parts. Note that the term "mutual impedance" is used instead of "mutual inductance"

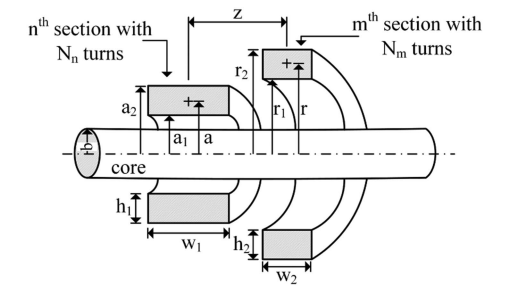


Fig. 2. Definition of parameters of two coils on a ferromagnetic core.

because it represents both the inductive and resistive components of the interaction between sections and the resistive term arises from eddy losses. $R_{\rm hv}$ and $R_{\rm lv}$ denote conductor resistances. Finally, the capacitances of the HV and LV sections, between one another, between the HV section and tank, as well as between the LV section and the core, are shown as $C_{\rm hv},\,C_{\rm lv},\,C_{\rm hl},\,C_{\rm hg},$ and $C_{\rm lg},$ respectively.

A. Inductances and Resistances

As mentioned above, the effects of the flux of the core and air components are considered separately in this paper. The frequency-dependent inductance and resistance of the winding sections is defined as follows:

$$Z_{nm} = Z_{1(nm)} + Z_{2(nm)} \tag{1}$$

in which $Z_{1(nm)}$ represents the contribution of the corecomponent flux to the sections' impedance, and $Z_{2(nm)}$ accounts for the effect of the air-component flux when the core is not present. This can be explained as follows. For lower frequencies, the flux is concentrated almost completely in the core; therefore, the values of the inductance and resistance are determined by $Z_{1(nm)}$, with $Z_{2(nm)}$ being negligible. However, with the increase in frequency, the core moves to an inactive state and affects the flux distribution only locally. In other words, there is no need to consider the effect of the core on the distribution of flux outside the core, and $Z_{2(nm)}$ can be obtained as if the transformer has an air core.

When calculating $Z_{1(nm)}$, magnetic flux lines do not intersect with the conductors' cross-section, so there is no need to consider eddy current losses in the conductors, and only losses in the core are important. However, skin and proximity effects on the conductors' impedance must be considered when calculating $Z_{2(nm)}$.

1) Core-Component Flux: Wilcox et al. [23] found an accurate expression for the self- and mutual inductances and resistances of coils wound on a solid ferromagnetic core by solving Maxwell's equations and defining appropriate boundary conditions. For coils on the same limb shown in Fig. 2, the solution is:

$$Z_{1(nm)} = jsN_nN_m \frac{\pi b^2}{\lambda} \left\{ \frac{2\mu_z I_1(mb)}{mbI_0(mb)} - \mu_1 \right\}$$
 (2)

$$m = \sqrt{s\mu_z\sigma} \tag{3}$$

Here, s is the Laplace operator, λ is the apparent magnetic circuit length seen by section n, μ_z and μ_1 ($\approx \mu_0$) are the magnetic permeabilities of the core in the axial direction and the medium outside of it, and σ is the conductivity of the core. I_0 and I_1 represent modified Bessel functions. It should be noted that the full Wilcox solution involves an infinite series that accounts for the magnetic flux outside the core, and (2) only accounts for the effects of the core-component flux. In our approach, we only use the leading term of the solution for the following reasons:

- For lower frequencies, the flux is mostly confined within the core, making the contribution of the magnetic field outside the core (represented by the infinite series) to be negligible.
- For higher frequencies, the core becomes inactive, and hence its influence on the magnetic field outside is minimal. As a result, the effects of the magnetic field outside the core are taken into account in $Z_{2(nm)}$, which also considers skin and proximity effects in conductors.

The frequency-dependent impedance $Z_{1(nm)}$ calculated in this way accounts for the eddy current losses in the core. By replacing s with the angular frequency ω , the values of mutual inductance and resistance between two coils at a particular frequency can be obtained:

$$R_{nm} = \text{real}\left(Z_{nm}\right) \tag{4}$$

$$L_{nm} = \frac{\mathrm{imag}\left(Z_{nm}\right)}{\omega} \tag{5}$$

Equation (2) is derived assuming a solid core. However, transformer cores are manufactured from thin laminated sheets to mitigate eddy current losses, typically with a width ranging from 0.25-0.85 mm. To apply (2) to real transformers, an equivalent solid core with the same amount of power loss and exhibiting the same magnetic behavior as the laminated core is required. For this, the following equation can be applied [24]:

$$\sigma = \frac{\sigma^* k}{n^2} \tag{6}$$

in which σ is the effective conductivity of the solid core in the plane orthogonal to the flux direction and is used in (3), σ^* is the conductivity of the material from which the lamination sheets are made, k is the stacking factor, and n is the number of sheets. Furthermore, the effective permeability can be obtained using (7) in which μ_z^* is the permeability of the laminated core [13], [25]:

$$\mu_z = k\mu_z^* + (1-k) \approx k\mu_z^*$$
 (7)

To investigate the accuracy of the equivalent conductivity method, simulations are carried out in COMSOL Multiphysics. For this, a laminated core consisting of 10 iron sheets with a width of 0.3 mm and its equivalent solid core are modeled. This is shown in Fig. 3. Table I summarizes the geometrical data for this case. When substituting the laminated core with an equivalent solid one, only the conductivity in the plane orthogonal to the flux direction is modified. Since the core has a toroidal shape, a new coordinate system is defined in COMSOL Multiphysics, which was consistently aligned with the core cross-section. This allows the computer program to distinguish the direction of

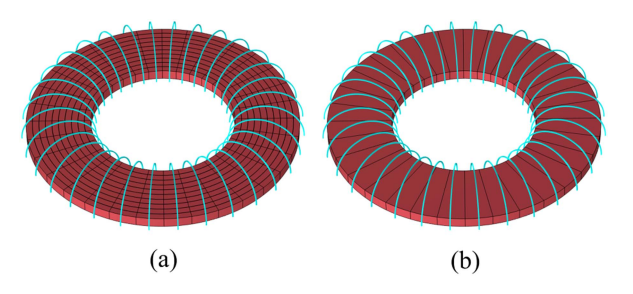


Fig. 3. The geometry of (a) a laminated core and (b) its equivalent solid one.

 $\label{eq:table_interpolation} TABLE\ I$ The Required Details of the Geometries Shown in Fig. 3

32
0.3
0.01
1.12e7
6.9/13.08
1
4000

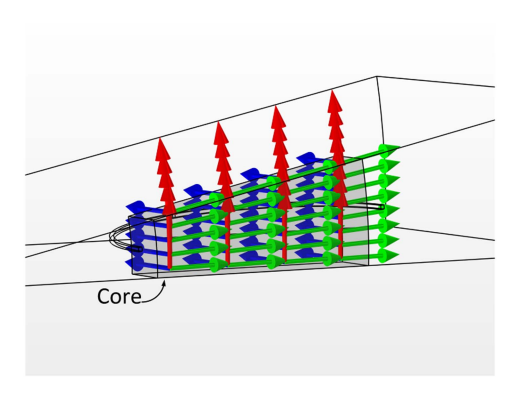


Fig. 4. The coordinate system used for the equivalent solid core.

conductivity, with specific values entered as a vector. This is shown in Fig. 4.

To maintain the computational efficiency, due to the symmetry of the core structure, only 1/32 of the entire model is simulated. Periodic boundary conditions are implemented to ensure that the reduced model accurately represents the behavior of the full core structure. A copper conductor is wound around the cores. By exciting the conductor with a current source, the average magnetic flux density at the core cross-sections is obtained for different frequencies, some of which are shown in Fig. 5. Since the magnetic flux distributions for both cases are the same, the parameters dependent on the flux, namely the inductance and resistance of the winding, should also be the same. Tables II and III compare inductance and resistance values between the laminated core and the equivalent solid core geometries. The agreement between the two models suggests that (6) and (7) can be applied to replace a laminated transformer core with an equivalent solid core without introducing large computation errors.

2) Air-Component Flux: Calculating the air-component impedance of the transformer sections, considering the skin

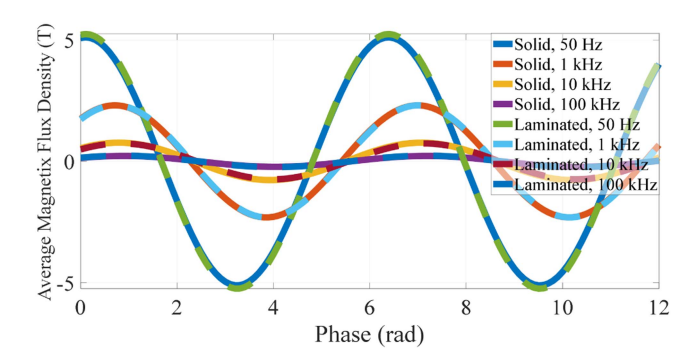


Fig. 5. Average magnetic flux density in laminated and equivalent solid cores.

TABLE II
INDUCTANCE OF THE WINDINGS IN FIG. 3

Frequency Hz	Inductance (lamination) mH	Inductance (solid) mH	Difference %
50	15.66	15.71	-0.31
100	15.01	15.11	-0.66
200	13.03	13.19	-1.22
1 k	5.20	5.34	-2.69
100 k	0.465	0.446	4.08
1 M	0.155	0.147	5.16

TABLE III
RESISTANCE OF THE WINDINGS IN FIG. 3

Frequency Hz	Resistance (lamination) $m\Omega$	Resistance (solid) $m\Omega$	Difference %
50	0.71	0.69	-2.24
100	2.17	2.07	-4.60
200	6.69	6.52	-2.54
1 k	29.01	29.92	-3.13
100 k	341.93	338.86	-0.89
1 M	1089.70	1070.7	-1.10

and proximity effects in conductors, is challenging due to the complex nature of these phenomena. The skin effect causes the alternating current to be distributed unevenly within the conductor, increasing the effective resistance at higher frequencies. Meanwhile, the proximity effect results from the magnetic fields generated by neighboring conductors, further altering the current distribution and impedance. These factors make it difficult to model the air-component impedance accurately, and therefore, sophisticated analytical or numerical techniques are required to account for the intricate electromagnetic interactions within the transformer windings.

The per unit (p.u.) length AC impedance Z_{ac} for a round conductor can be calculated using (8) [25]:

$$Z_{ac} = R_{dc} + \frac{j\omega\bar{A}}{I}$$
 (8)

in which, $R_{\rm dc}$ is the p.u. DC resistance, \bar{A} is the average magnetic vector potential over the cross-section, I is the AC current, and ω is the angular frequency. For a group of conductors, the calculation of the magnetic vector potential \bar{A} involves considering the effects of all other conductors within the system. This process requires the magnetic vector potential in the air surrounding the conductor of interest to be divided into two components:

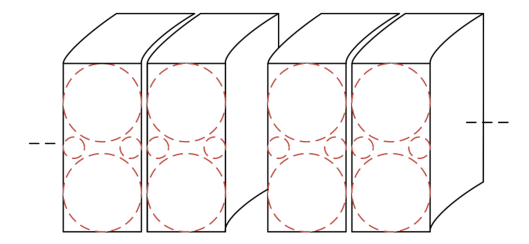


Fig. 6. Replacing rectangular conductors with several round ones.

- Received Part: Represents the influence of external sources, including current in nearby conductors and the other magnetic field.
- 2) *Emitted Part:* Represents the effect due to currents within the conductor of interest.

The resultant system of equations is formed based on the boundary condition at the surface of the conductor, which requires the received magnetic vector potential to equal a coefficient times the sum of the emitted parts from all other conductors in the system. Using the established set of equations, the magnetic vector potential in both the air and the conductor of interest can be determined. This method takes into account the interactions between all conductors, from both direct and indirect contributions to the magnetic field. A brief mathematical derivation of this approach is provided in Appendix B. More details on the mathematical derivation and solution can be found in [25]. The proposed 2-D analytical method in [25] is extended in this paper to handle rectangular conductors by modeling each conductor as several parallel round conductors, as shown in Fig. 6. Conceptually, the rectangular conductor can be treated as a series of parallel round conductors, which allows capturing the essential high-frequency effects, such as skin and proximity effects, where current tends to flow on the surface. By using a minimal number of round conductors, the surface is effectively covered, providing a balance between accuracy and computational efficiency. This approach ensures that the high-frequency behavior is well-represented without introducing unnecessary complexity. The major advantage of this approach is its ability to compute the AC impedance for arbitrary winding configurations, regardless of the spatial distribution of conductors. Furthermore, it is very efficient in terms of the required computation time and processing power.

To validate the accuracy of the method, comparisons with FEM are carried out. To keep the computation power required by FEM approach reasonable, ten disks of the HV winding of the transformer are modeled by COMSOL Multiphysics. Figs. 7 and 8 show the self- and mutual resistances and inductances associated with the first disk, respectively, obtained from the analytical approach and FEM. In the analytical approach, each turn is replaced by four parallel round conductors. As can be seen, the agreement between the results obtained from FEM and the analytical formula is substantial.

To assess the method's efficiency, the computation time for each frequency point is measured across 644 sections, corresponding to the number of sections for one phase of the three-phase transformer model. The total computation time for

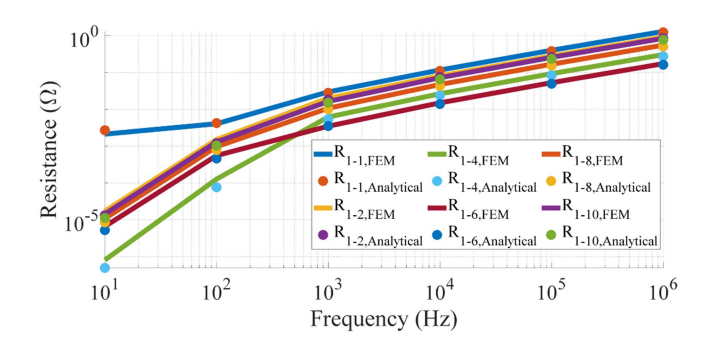


Fig. 7. Resistance values associated with the first disk obtained from analytical formulas and FEM.

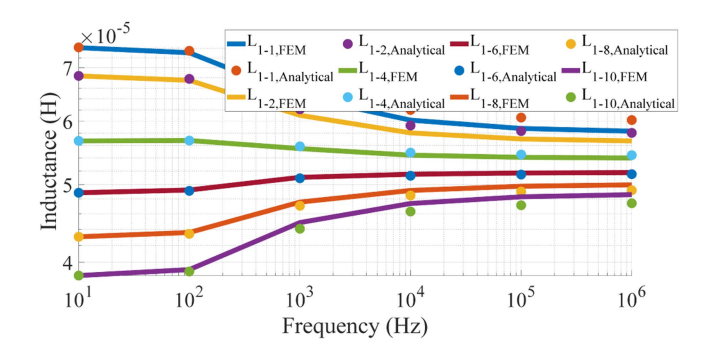


Fig. 8. Inductance values associated with the first disk obtained from analytical formulas and FEM.

this analysis is around 3 hours, using a personal computer. In contrast, performing a similar analysis for just one section of a transformer with 213 sections (compared to 644 sections in the analytical method) using FEM requires between 42 and 164 hours, depending on the frequency range [26]. The FEM analysis is conducted on a cluster of computers, each with a Pentium i7 CPU and 8 GB of RAM. Moreover, to obtain values for all 213 sections using FEM, the simulation would need to be run 213 times [26], significantly increasing the total computational time. In contrast, the analytical method allows for the parameters of all sections to be obtained in a single run, demonstrating a substantial advantage in terms of time efficiency.

3) Comparative Impedance Analysis: Air-Component Flux Versus Core-Component Flux: To understand the effects of the core- and air-component fluxes on the impedance of the sections, the inductance and resistance of the first section of the three-phase transformer are plotted in Figs. 9 and 10, respectively, considering each effect separately. From these figures, one might conclude that the effect of the core-component flux is predominant even in the high-frequency range. However, as it is shown in the following sections, this is not the case for all conditions. In fact, in the high-frequency region, air-component flux becomes the main influencing factor.

B. Capacitances

In addition to modeling the resistances and inductances, the precise calculation of capacitances within the transformer is crucial for conducting a comprehensive electromagnetic transient

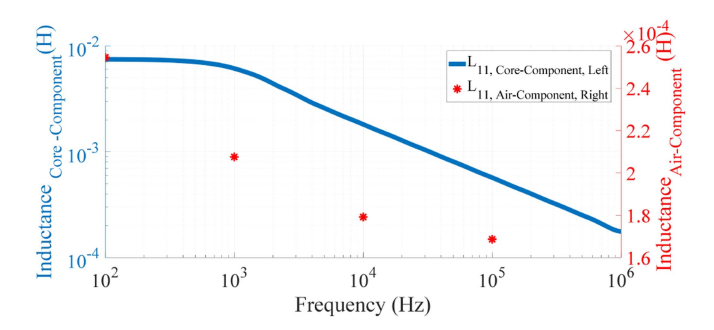


Fig. 9. The inductance of the first transformer's disk obtained by taking into account different flux components.

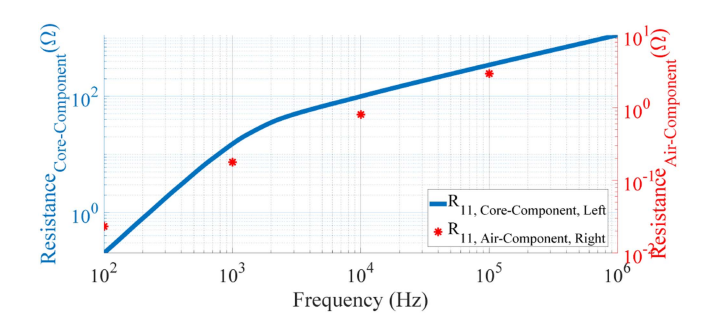


Fig. 10. The resistance of the first disk of the transformer obtained considering different flux components.

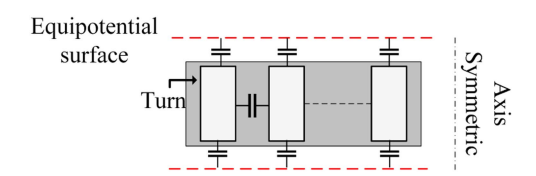


Fig. 11. An illustration of a winding section and equipotential lines.

analysis. Depending on the degree of discretization, the capacitances incorporated into the model are either physical capacitances depending on the physical dimensions and arrangement of the windings, or equivalent capacitances, which are derived using the energy method. The latter approach is particularly suitable when multiple conductors are grouped and considered a single section. It is based on the electric field distribution and the stored energy within the transformer. The procedure to derive these capacitances is elaborated below.

1) Equivalent Capacitance Based on the Energy Method: The equivalent capacitance can be obtained based on the energy stored in the equipotential area between the sections. In [7], it was shown that this approach can be applied to fast transient voltage distribution analysis in transformer windings. For continuous disk windings, by assuming a linear voltage distribution along the winding and considering the equipotential surfaces, see Fig. 11, the equivalent capacitance can be obtained as [19]:

$$C_{hv} = \frac{4}{3}C_{dd} + \frac{N_t - 1}{N_t^2}C_{tt} \tag{9}$$

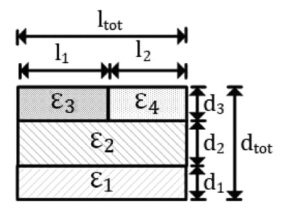


Fig. 12. The geometry used to calculate effective permittivity for different configurations.

In (9), C_{tt} and C_{dd} are the capacitances between two adjacent turns and the total capacitance between two adjacent disks, respectively, whilst N_t is the number of turns in each disk. C_{tt} and C_{dd} can be obtained by (10) and (11) [19]:

$$C_{tt} = \frac{\varepsilon_0 \varepsilon_r 2\pi R_{ave}(h+d)}{d} \tag{10}$$

$$C_{dd} = \frac{\varepsilon_0 \varepsilon_r \pi \left(R_{out}^2 - R_{in}^2 \right)}{d} \tag{11}$$

in which R_{ave} , R_{out} , and R_{in} are the mean, outer, and inner radius of the disk, respectively. h is the height of the conductor without insulation, ε_r represents equivalent relative permittivity, and d is the distance between conductors in the geometry of interest. It should be noted that ε_r in (10) is not the same as ε_r in (11), as each value depends on the specific geometry of interest. Fig. 12 illustrates an example of different insulation types for a given configuration, and the equivalent permittivity for this configuration can be obtained by (12). This configuration serves as a reference to calculate the equivalent permittivity in (10) and (11).

For different configurations of the transformer windings, such as internally shielded or interleaved discs, the reader is advised to refer to Chapter 5 of [9] where suitable formulas for series capacitance calculations are presented.

$$\frac{1}{\varepsilon_r} = \frac{1}{\varepsilon_1} \frac{d_1}{d_{tot}} + \frac{1}{\varepsilon_2} \frac{d_2}{d_{tot}} + \frac{1}{\varepsilon_3 \frac{l_1}{l_{tot}} + \varepsilon_4 \frac{l_2}{l_{tot}}} \frac{d_3}{d_{tot}}$$
(12)

2) Geometrical Capacitance: The associated capacitances in this case can be obtained by employing well-known formulas for parallel plate or cylindrical capacitors.

III. ADMITTANCE MATRIX OF THE TRANSFORMER

Having all the required elements, the admittance matrix of the transformer can be obtained using (13) and (14)

$$\mathbf{Y} = \mathbf{\Gamma} + \mathbf{j}\omega\mathbf{C} \tag{13}$$

$$\Gamma = \mathbf{k} \left(\mathbf{R} + \mathbf{j} \omega \mathbf{L} \right)^{-1} \mathbf{k}^{\mathrm{T}}$$
 (14)

where Γ , R, L, and C are the nodal impedance, resistance, inductance, and capacitance matrices, respectively. k is the incidence matrix, T represents the transpose operation, and ω is the angular frequency. The Impedance matrix \mathbf{Z} can be obtained by inverting the admittance matrix \mathbf{Y} . The procedure for obtaining these matrices is elaborated here below.

A. Resistance and Inductance Matrices

The inductance and resistance matrices are branch matrices with diagonal elements representing the self-parameters of the sections, and off-diagonal elements are the mutual parameters between them. The elements of these matrices are frequency-dependent, and therefore, they need to be updated at each frequency point.

B. Incidence Matrix

This matrix transforms the inductance and resistance branch matrices into nodal ones. Different winding connections (Δ and Y) can be defined through the appropriate construction of the k matrix. The elements of this matrix are 0, -1, and 1. Specifically, an element is:

- 1 if an element starts at a node,
- −1 if an element ends at a node.
- 0 if the element is not connected to the node.

C. Capacitance Matrix

The capacitance matrix is nodal, and its diagonal element i is the sum of all elements connected to node i. The off-diagonal element i, j represents the capacitance between these two nodes with the negative sign.

IV. TRANSFORMER CHARACTERISTICS AND MODEL VERIFICATION

When assuming linearity, the relationship between voltages ${\bf V}$ and currents ${\bf I}$ at different nodes of transformer windings can be represented by:

$$V = ZI \tag{15}$$

When node j is excited by current I_j , the node voltages can be computed according to [27]:

$$\begin{bmatrix} V_1 \\ \vdots \\ V_j \\ \vdots \\ V_n \end{bmatrix} = \begin{bmatrix} Z_{11} & Z_{12} & \dots & Z_{1n} \\ \vdots & \vdots & \ddots & \vdots \\ Z_{j1} & Z_{j2} & \dots & Z_{jn} \\ \vdots & \vdots & \ddots & \vdots \\ Z_{n1} & Z_{n2} & \dots & Z_{nn} \end{bmatrix} \begin{bmatrix} 0 \\ \vdots \\ I_j \\ \vdots \\ 0 \end{bmatrix}$$
(16)

To verify the accuracy of the proposed approach, three case studies are conducted; the first one is for an HV test winding and the other two are for one- and three-phase transformers. The HV winding provides an initial validation case, whilst the cases with the power transformer represent a more complex and practical application. For all cases, the model results are compared with measurements over a wide frequency range and under transient conditions. The verification process and findings are detailed in the following subsections.

A. HV Coil

Firstly, the method is applied to the HV winding to validate the modeling approach for a simpler geometry before moving to the more detailed transformer case study. The HV winding

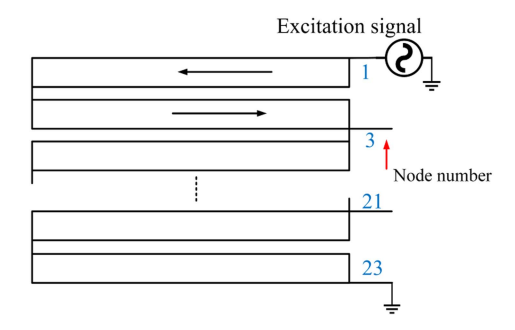


Fig. 13. An illustration of the HV winding. Arrows show the direction of the winding.

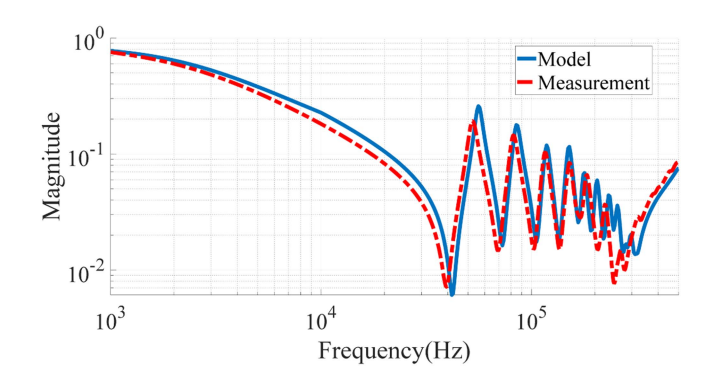


Fig. 14. The ratio of the voltage at node 3 and the terminal voltage.

consists of 22 disks, as shown in Fig. 13, where each disk is considered as one section in the model. The associated inter-disk capacitances are calculated based on the energy method. The coil includes wound-in electrostatic shields between the turns. These shields are designed to improve the capacitive voltage distribution, enhancing the overall performance and reliability of the transformer by mitigating non-linear voltage distribution across the winding. The procedure to accurately account for these shields in the model is detailed in [28]. Since the coil has been in open air for an extended period, the paper insulation has absorbed significant moisture over time. The moisture effect is considered in terms of insulation losses, however, the measurements show no change in the permittivity of the insulation. To incorporate dielectric loss effects, (17) is used based on [29]:

$$\tan \delta = 1.082 \times \omega \times 10^{-8} + 40 \times 10^{-3} \tag{17}$$

To validate the model, the voltage distribution along the winding is measured at various terminals and for different frequencies using an Omicron Bode 100 instrument. These measurements are conducted with 50 Ω terminating resistances to mitigate the effects of wave reflection. Figs. 14 and 15 compare two sets of these measured voltages at nodes 3 and 13 with the model. The close agreement between the modeled and simulated results shows the accuracy of both the modeling approach and the determination of associated parameters.

Transient studies are also conducted by applying triangular voltage pulses with 5 μ s and 3 μ s rise times and 0.3 μ s fall times, as shown in Fig. 16. The time-domain voltage responses at nodes

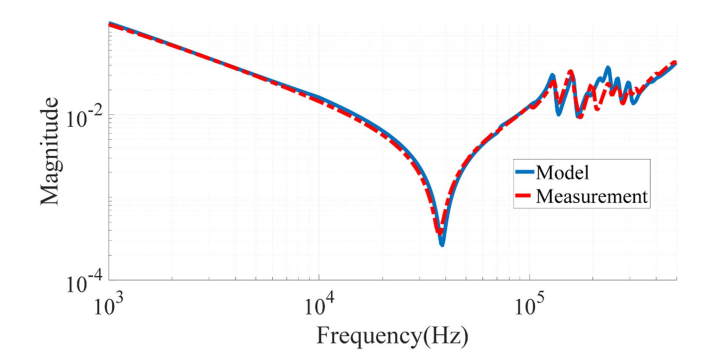


Fig. 15. The ratio of voltage at node 13 and the terminal voltage.

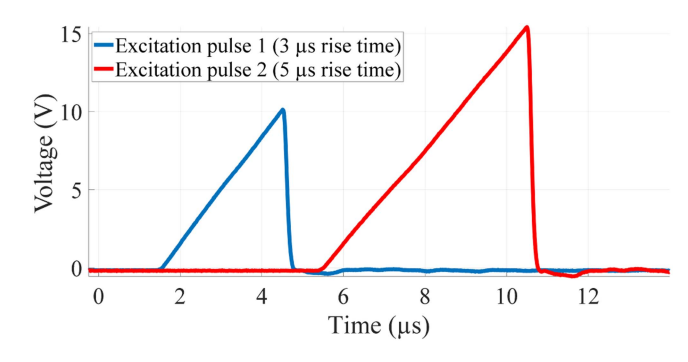


Fig. 16. Excitation signals applied to the HV coil.

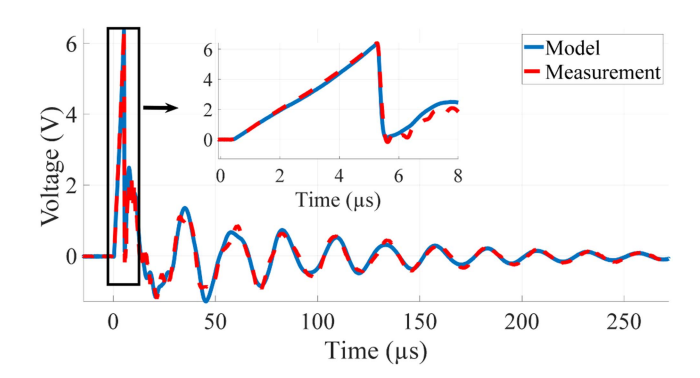


Fig. 17. Node 13 voltage - model vs. measurement (5 μs rise time).

13 and 15 within the winding are measured and compared to the model, and the results are shown in Figs. 17 and 18, respectively. The results show good agreement, with the oscillating frequency of 40 kHz in both cases matching the first anti-resonance point predicted by the model and measurements.

A separate model utilizing constant inductance values is created to highlight the importance of incorporating frequency-dependent inductances. The inductances are derived according to [25], while skin and proximity effects in the conductors are ignored. When compared to the measurements, apart from differences in magnitude, this simplified constant-parameter model exhibited noticeable phase-shifting errors, underlying the need for a more accurate variable inductance formulation in the full model, which is also highlighted in CIGRE workgroup A2/C4.52 [9]. For example, the voltage of node 15 obtained by the constant parameter model is shown in Fig. 18.

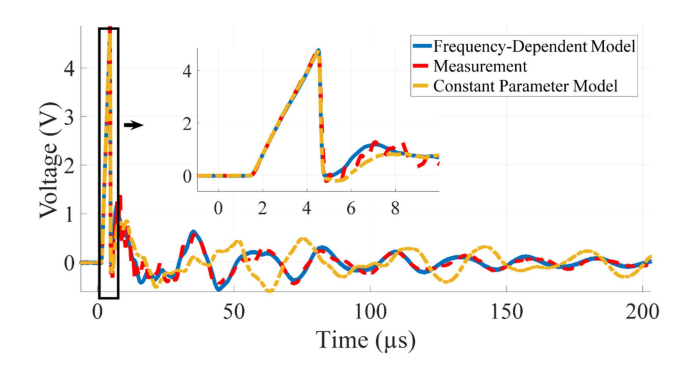


Fig. 18. Node 15 voltage - model vs. measurement (3 µs rise time).

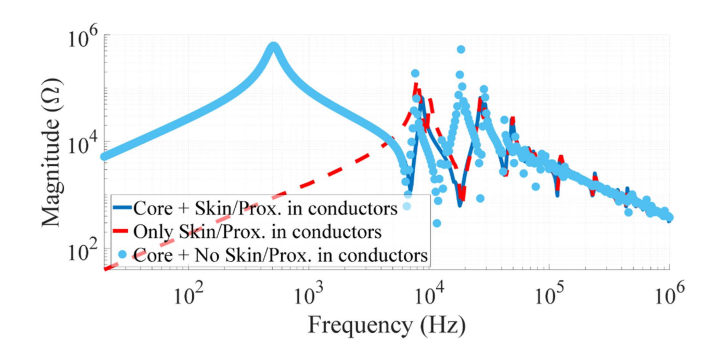


Fig. 19. Terminal impedance of the HV winding of phase R.

B. Transformer Model

The second case study examines a three-phase transformer with a power rating of 48 MVA. Apart from the regular HV and LV windings, this transformer has a tap changer consisting of two coarse layer-type windings and one fine multi-start winding, totaling 23 taps. Except for the HV winding, where each disk is considered as one section, for other windings, each turn is considered as one section.

To elucidate the impact of the core on the high-frequency behavior, the complete transformer model is obtained by considering core- and air-component effects on the conductors'impedance. Fig. 19 shows the terminal impedance of the HV winding of phase R obtained from these three models. This figure shows that when skin and proximity effects are taken into account, high-frequency transformer responses with and without considering the core are the same. This is because significant phase shifts between different winding sections appear as the frequency increases, causing the effects of the core-component flux to be eliminated. This phenomenon implies that the net magnetic motive force (MMF) generated by the windings would be nearly zero, resulting in negligible flux within the core. The details of this mechanism are explained by the authors in [30]. It should be noted that this phenomenon has nothing to do with skin depth, as evidenced by Fig. 9. Also, when skin and proximity effects in conductors are ignored, a different behavior at higher frequencies occurs, highlighting the importance of considering these effects in conductors.

Significant phase-shift implies that the difference between the leakage impedance of different sections dictates the highfrequency response. The flux cancellation means that discarding

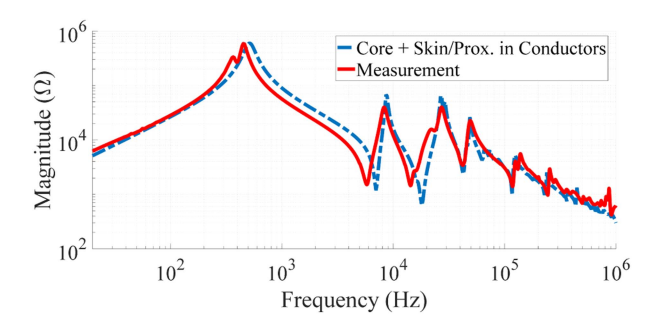


Fig. 20. Comparison of measured and simulated terminal impedance of the transformer's HV winding of phase R.

skin and proximity effects would introduce significant errors in the high-frequency behavior. Not only is a considerable portion of the losses ignored but also the frequencies of the resonance points would also differ from actual ones, as the difference between leakage impedance values plays a crucial role. While the error in the absolute values might not be significant, the error in the difference between leakage impedances can be substantial. On the other hand, the low-frequency behavior is impacted only by the core. Therefore, core losses must be calculated accurately to obtain the correct initial conditions for transient simulations. By considering the eddy current losses for both the core and the conductors the accuracy of the model within the broad frequency range is considerably improved.

To validate the model, the transformer frequency response is measured and compared with the model. On-site frequency-sweep measurements are performed using a DV FRA500 instrument. Fig. 20 compares the HV terminal impedance of Phase R of the transformer obtained by the model with the measurement taken at the lowest tap position. As can be seen, there is a good agreement between the model and measurement. Having the model validated, it can be used for transient studies by implementing it in an EMT-based software environment.

To validate the accuracy and robustness of the developed model, additional analysis is carried out for the one-phase transformer as reported by CIGRE JWG A2/C4.52. The results of this analysis are presented in Appendix A.

V. EMT-BASED SOFTWARE IMPLEMENTATION

Considering the large number of sections and admittance matrix size, it is not possible to implement the model directly for transient studies. Instead, firstly, the admittance matrix should be reduced to a smaller order. The Kron reduction method is applied to reduce the initial order of the matrix to an arbitrary low-order matrix that provides the same information from the original matrix, only for the nodes of interest. For this, (18) can be applied to the admittance matrix:

$$Y'_{ij} = Y_{ij} - \frac{Y_{ik}Y_{jk}}{Y_{kk}} \qquad i, j \neq k$$
 (18)

in which k is the row to be eliminated.

By finding the amplification factor (AF), the critical nodes with the highest voltage can be identified, and only these nodes,

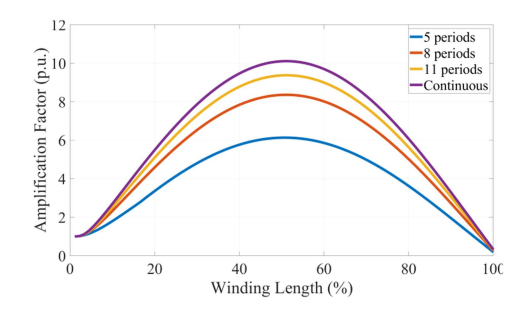


Fig. 21. Voltage amplification in the HV winding of the three-phase transformer obtained at 18 kHz.

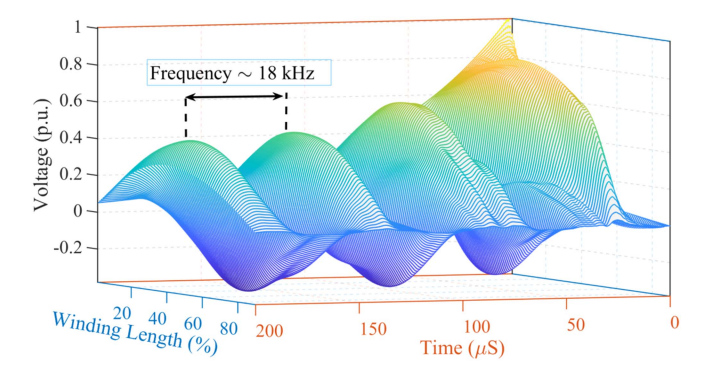


Fig. 22. Voltage distribution in the HV winding of the transformer upon applying standard lightning impulse.

along with the terminal nodes, are retained, whilst the remaining nodes will not be observed as they are exposed to lower voltages. The AF when the excitation is applied to the terminal node i is defined as [27]:

$$AF = \frac{V_{ij}}{V_{ii}} = \frac{Z_{ij}}{Z_{ii}} \tag{19}$$

where V_{ii} is the terminal voltage, and V_{ij} is the voltage of node j. Fig. 21 shows the voltage amplification in the HV winding of the studied transformer for sinusoidal excitations with the frequency of 18 kHz and different durations. This frequency corresponds to the second anti-resonance point observed from the terminal impedance (see Fig. 19). As observed, the highest voltage amplification occurs in the middle of the winding, with values reaching up to 10 p.u.

Alternatively, only the terminal nodes can be observed and the corresponding voltages of these nodes can be computed. By applying (16), the voltages of interest can be computed firstly in the frequency domain, and afterward, by applying the modified Fourier transform, they can be computed in the time domain [31]. In this way, the detailed voltage distribution along the transformer windings can be obtained. Fig. 22 shows the complete voltage distribution in the HV winding of the transformer obtained in this way when a standard lighting impulse of $1.2/50~\mu s$ is applied to its terminal. In this case, the maximum voltage in the middle of the winding can reach 0.8~p.u., which, considering the amplitude of the actual lightning signals, is quite high. Furthermore, the voltage oscillates with a frequency of 1.8~kHz, corresponding to the second anti-resonance point. This

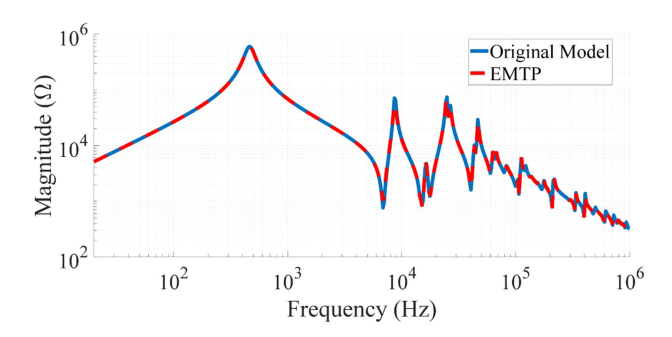


Fig. 23. The input impedance of phase R obtained from the reduced model implemented in EMTP-RV and the original model.

occurs because this point results in the highest amplification factor, making its effect more dominant in the waveform.

After model reduction, the vector fitting and passivity enforcement algorithms [32], [33], [34], [35], [36] are applied to the admittance matrix. In this way, the obtained model can be implemented in an EMT software environment. Fig. 23 compares the terminal impedance of phase R of the reduced model implemented in EMTP with the original model. It should be noted that these characteristics are obtained at the maximum tap position and the order of the admittance matrix is reduced from 1944 to 6 terminals.

VI. CONCLUSION

This paper presents a high-frequency transformer model based on analytical formulas, that take into account the frequency-dependent transformer behavior. By considering eddy current losses in both the conductors and core, and using accurate 2D analytical formulas to compute skin and proximity effects, the proposed approach offers a precise calculation of the winding sections' impedance. This model also accounts for core eddy current losses, ensuring accurate transient analysis where initial conditions and low-frequency behavior are also crucial.

Our findings demonstrate that core effects dominate at low frequencies, while high-frequency characteristics are primarily influenced by leakage impedances. This behavior is explained by considering the significant phase shifts along the windings at high frequencies. Consequently, the net magneto-motive force (MMF) generated by the windings becomes negligible, and the effects of air-component flux become more pronounced at higher frequencies. The model's accuracy is validated through extensive comparisons with time- and frequency-domain measurements, confirming its robustness. This ensures reliable simulations of scenarios like inter-turn and inter-disk voltage calculations.

Additionally, a reduced-order transformer model is developed using admittance matrix reduction. This technique enables efficient computation of voltages at specific points of interest while maintaining the accuracy of the original model. The reduced-order model preserves the detailed interactions between the core and conductors, making it suitable for high- and low-frequency transient analysis. Moreover, its implementation in an EMT software tool is straightforward and efficient, offering a practical solution for different applications.

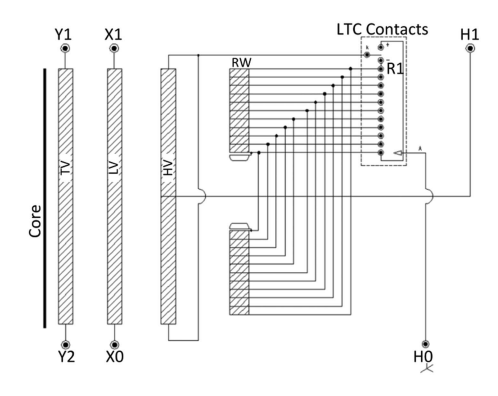


Fig. 24. Internal connections and labeling of the one-phase transformer according to CIGRE JWG A2/C4.52 [37].

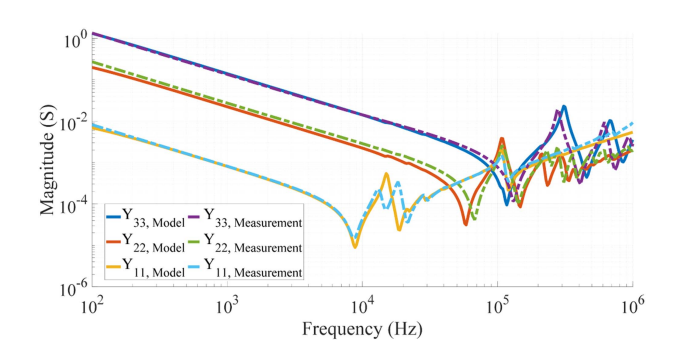


Fig. 25. Comparison of admittance matrix elements for the CIGRE transformer: model vs. measurements.

APPENDIX A BENCHMARK STUDY USING DATA PROVIDED BY CIGRE JWG A2/C4.52

In addition to the previous analysis, an analysis is carried out for one of the transformers published in CIGRE JWG A2/C4.52 Technical Brochure No. 904. Specifically, we modeled the single-phase transformer reported in the brochure. In this model, each turn of the tertiary (TV) winding and each disk of the low-voltage (LV) winding is treated as a single section, while each double disk of the high-voltage (HV) winding and every 10 disks of the regulating winding (RW) are considered as individual elements. The studied transformer is without oil, thus moisture absorption could impact the insulation properties. Therefore, dielectric losses are considered by using (17), given the lack of dissipation factor data in the brochure. Fig. 24 presents the transformer internal connections and labeling, with terminals numbered as follows: 1 (H1), 2 (X1), 3 (Y1), and 4 (Y2).

Fig. 25 shows the admittance characteristics obtained from both the model and measurements. It is worth mentioning that the measurements are provided by the CIGRE JWG A2/C4.52 working group as reported in [37], [38]. Additionally, timedomain simulations are performed to evaluate the accuracy of the developed model. For the first case, a lightning impulse is applied to the HV terminal (H1), and the responses at X1, Y1, and R1 are recorded while H0 and X0 are grounded, and the TV winding is floating. For the second case, the excitation is applied

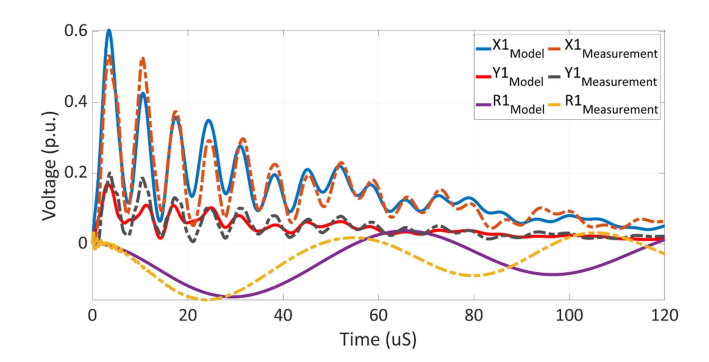


Fig. 26. Responses at terminals X1, Y1, and R1 to a lightning impulse applied at HV terminal H1.

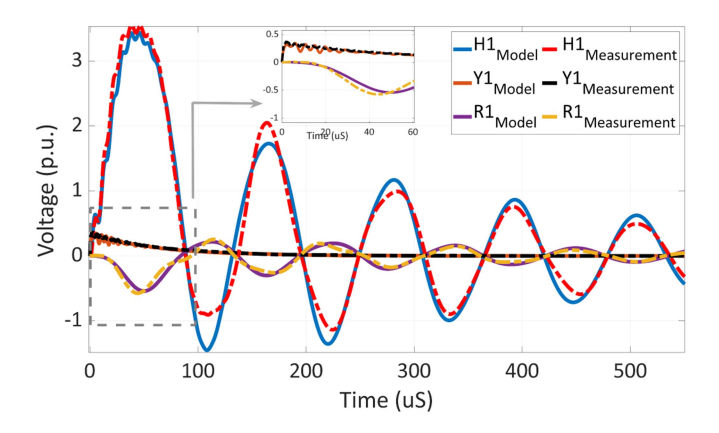


Fig. 27. Responses at terminals H1, Y1, and R1 to a lightning impulse applied at LV terminal X1.

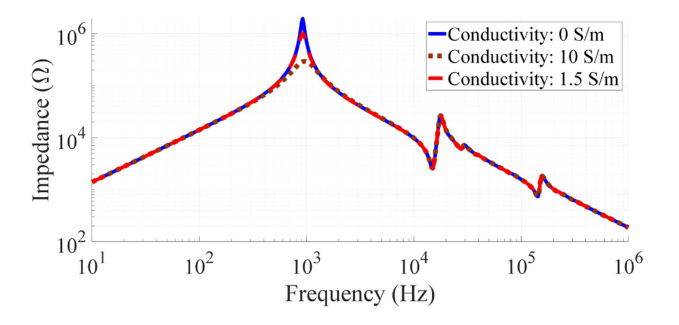


Fig. 28. HV winding impedance obtained with different equivalent conductivity values.

to X1, with responses measured at H1, Y1, and R1 under the same conditions. These comparisons are shown in Figs. 26 and 27, respectively, demonstrating a good agreement between the modeled and measured responses.

Furthermore, to investigate the effects of core losses on the transformer response, the impedance of the HV winding of the CIGRE transformer is plotted for three different conductivity values: 10, 1.5, and 0 S/m, as shown in Fig. 28. Since the equivalent conductivity value is typically below 10 S/m for power transformers, these changes primarily affect the amplitude of the resonance frequency in the low-frequency region, as shown in Fig. 28.

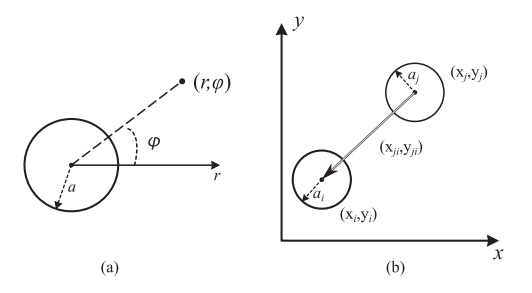


Fig. 29. Illustration of coordinates used in the 2D analysis, (a) polar coordinates for a single round conductor, (b) Cartesian coordinates for multiple conductors.

APPENDIX B

A BRIEF INTRODUCTION TO THE IMPEDANCE CALCULATION OF AIR-COMPONENT FLUX

The 2D analysis is briefly introduced here. For simplicity, the derivation is restricted to first-order harmonic terms. A comprehensive mathematical derivation can be found in [25]. As illustrated in Fig. 29, the 2D analysis utilizes polar and 2D Cartesian coordinates, both originating at the round conductor center. For polar coordinates, the magnetic vector potential inside the conductor is represented by (20). Additionally, the magnetic vector potential A around the elements is defined by (21).

$$\nabla^2 \mathbf{A} - j\omega\sigma\mu\mathbf{A} = \mu\sigma\nabla\phi \tag{20}$$

$$\nabla^2 \mathbf{A}(r,\varphi) = 0 \tag{21}$$

The general solution of (20) is expressed by (22), where A_0 represents the particular solution and is a constant. The term J_n denotes the first-kind Bessel function, with n as the order, a as the element's radius, and κ defined as $\sqrt{-i\omega\sigma\mu}$.

$$\mathbf{A}_{c}(r,\varphi) = A_0 + \alpha_0 J_0(\kappa r) + J_1(\kappa r)(\alpha_1 \cos \varphi + \beta_1 \sin \varphi)$$
(22)

The general solution of (21) is provided in (23). The coefficient C represents the vector potential resulting from currents in other elements, while coefficient D corresponds to the net current I flowing through the element. The coefficients A', A'', B' and B'' are associated with the first-order harmonics.

$$A(r,\varphi) = C + D\ln(r) + \left(rA' + \frac{A''}{r}\right)\cos(\varphi) + \left(rB' + \frac{B''}{r}\right)\sin(\varphi)$$
(23)

Subsequently, the boundary conditions at the conductor's surface are defined in (24).

$$\mu_{c}H_{r_c}|_{r=a} = \mu_{0}H_{r_air}|_{r=a}$$

$$H_{\varphi_c}|_{r=a} = H_{\varphi_air}|_{r=a}$$

$$A_{z_c}|_{r=a} = A_{z_air}|_{r=a}$$
(24)

After equating the same harmonic terms in (23) and (22), the relationships in (25) are obtained.

$$D = -\frac{\mu_0 I}{2\pi} \alpha_0 = -\frac{D}{\kappa a J_1(\kappa a)}$$

$$A_1''|B_1'' = \frac{a^2 J_2(\kappa a)}{J_0(\kappa a)} A_1'|B_1'$$

$$\alpha_1|\beta_1 = \frac{2}{\kappa a^2 J_2(\kappa a)} A_1''|B_1''$$

$$A_0 + \alpha_0 J_0(\kappa a) = C + D \ln a. \tag{25}$$

When there are multiple circular elements, as illustrated in Fig. 29(b), each element has a magnetic vector potential solution in the form of (23), with each function represented in polar coordinates of the respective element. Then, the functions are transformed into 2D-Cartesian coordinates. Given that the value of Green's function for the Laplace equation is inversely proportional to the distance, the expression in (23) is divided into two parts based on the relation between the value and distance. The first part consists of coefficients D, A'', and B'' generated from the source within the element. The second part consists of other coefficients originating from sources external to the component. By matching the second part of an element with the first part from other elements within the same coordinates, a relationship such as (26) can be established. Here, subscripts iand j indicate different conductors, while x_{ii} and y_{ii} represent the coordinate transformations from element i to element i in the x and y directions. Through solving the matrix, the coefficients for 2D cases can be obtained.

$$C_{i} + \sum_{j \neq i} A''_{j} \frac{x_{ji}}{x_{ji}^{2} + y_{ji}^{2}} + \sum_{j \neq i} B''_{j} \frac{y_{ji}}{x_{ji}^{2} + y_{ji}^{2}}$$

$$= \sum_{j \neq i} \frac{D_{j}}{2} \ln (x_{ji}^{2} + y_{ji}^{2})$$

$$A'_{i} + \sum_{j \neq i} A''_{j} \frac{x_{ji}^{2} - y_{ji}^{2}}{(x_{ji}^{2} + y_{ji}^{2})^{2}} + \sum_{j \neq i} B''_{j} \frac{2x_{ji}y_{ji}}{(x_{ji}^{2} + y_{ji}^{2})^{2}}$$

$$= \sum_{j \neq i} D_{j} \frac{x_{ji}}{x_{ji}^{2} + y_{ji}^{2}}$$

$$B'_{i} + \sum_{j \neq i} A''_{j} \frac{2x_{ji}y_{ji}}{(x_{ji}^{2} + y_{ji}^{2})^{2}} - \sum_{j \neq i} B''_{j} \frac{x_{ji}^{2} - y_{ji}^{2}}{(x_{ji}^{2} + y_{ji}^{2})^{2}}$$

$$= \sum_{j \neq i} D_{j} \frac{y_{ji}}{x_{ji}^{2} + y_{ji}^{2}}$$

$$= \sum_{j \neq i} D_{j} \frac{y_{ji}}{x_{ji}^{2} + y_{ji}^{2}}$$

$$(26)$$

After all coefficients in (23) are determined, the relationship between the impedance and mathematical coefficients is needed. The relation between potential ϕ , current I, and average vector potential \bar{A} is described in (27). Equation (8) is derived by dividing both sides by I.

$$-\nabla \phi = R_{\rm dc}I + j\omega \bar{A} \tag{27}$$

 \bar{A} is presented in (28), derived by integrating (22) over the conductor's surface. By using the relationships established in (25), (28) is obtained.

$$\iint A_{\rm c} dS = \int_0^a \int_0^{2\pi} A_{\rm c} r d\varphi dr$$

TABLE IV
THREE-PHASE TRANSFORMER PARAMETERS

Transformer	Rated Power (MVA) Rated Voltage (kV) OLTC	48 150/11.2 +12/-11 steps of 2.5 kV
LV	Type Number of layers Number of turns	Layer 4 142
HV	Type Number of disks Number of turns	Disk 90 900
G1	Type Number of layers Number of turns	Layer 1 144
G2	Type Number of layers Number of turns	Layer 1 144
FW	Type Number of steps Number of turns	Multi-start 7 126

TABLE V HV Coil Parameters

Number of Disks	22
Number of turns per disk	40
Conductor dimensions	$1.8 \text{ mm} \times 8 \text{ mm}$
Conductor insulated dimensions	$3.11 \text{ mm} \times 9.31 \text{ mm}$
Radial build	125.5 mm
Inner diameter	750 mm
Outer diameter	1001 mm
Vertical distance between disks	4 mm
Number of disks with 3 turns of shields	4
Number of disks with 2 turns of shields	4
Number of disks with 1 turns of shields	4
Number of disks with no shields	10

$$= C + D\ln(a) - \frac{DJ_2(\kappa a)}{\kappa a J_1(\kappa a)} \quad (28)$$

APPENDIX C TRANSFORMER AND COIL DESIGN DATA

Tables IV and V provide the details of the three-phase transformer and coil. In Table IV, G1, G2, and FW refer to the tap changer windings of the transformer. The transformer tap changer comprises three windings: two coarse windings (G1 and G2) and one fine winding (FW). These windings enable voltage adjustment and regulation through the tap changer mechanism.

ACKNOWLEDGMENT

The authors thank Royal Smit Transformers B.V. for providing a test winding and data for this research project, DSO Alliander/Qirion for the support in performing transformer field measurements, and TSOs TenneT and National Grid for the inspirational discussions. The authors also thank anonymous reviewers for their valuable comments and suggestions, which have significantly improved the manuscript.

REFERENCES

- A. Abu-Siada and S. Islam, "A novel online technique to detect power transformer winding faults," *IEEE Trans. Power Del.*, vol. 27, no. 2, pp. 849–857, Apr. 2012.
- [2] M. Bagheri, M. S. Naderi, and T. Blackburn, "Advanced transformer winding deformation diagnosis: Moving from off-line to on-line," *IEEE Trans. Dielectrics Elect. Insul.*, vol. 19, no. 6, pp. 1860–1870, Dec. 2012.
- [3] E. E. Mombello, Á. Portillo, and G. A. D. Flórez, "New state-space white-box transformer model for the calculation of electromagnetic transients," *IEEE Trans. Power Del.*, vol. 36, no. 5, pp. 2615–2624, Oct. 2021.
- [4] G. Ramarao and K. Chandrasekaran, "Calculation of multistage impulse circuit and its analytical function parameters," *Int. J. Pure Appl. Math*, vol. 114, pp. 583–592, 2017.
- [5] R. Aghmasheh, V. Rashtchi, and E. Rahimpour, "Gray box modeling of power transformer windings for transient studies," *IEEE Trans. Power Del.*, vol. 32, no. 5, pp. 2350–2359, Oct. 2017.
- [6] M. Gunawardana, F. Fattal, and B. Kordi, "Very fast transient analysis of transformer winding using axial multiconductor transmission line theory and finite element method," *IEEE Trans. Power Del.*, vol. 34, no. 5, pp. 1948–1956, Oct. 2019.
- [7] N. Abeywickrama, Y. V. Serdyuk, and S. M. Gubanski, "High-frequency modeling of power transformers for use in frequency response analysis (FRA)," *IEEE Trans. Power Del.*, vol. 23, no. 4, pp. 2042–2049, Oct. 2008.
- [8] M. Eslamian and B. Vahidi, "New equivalent circuit of transformer winding for the calculation of resonance transients considering frequency-dependent losses," *IEEE Trans. Power Del.*, vol. 30, no. 4, pp. 1743–1751, Aug. 2015.
- [9] CIGRE Technical Brochure 900, "High-frequency transformer and reactor models for network studies, Part A: White-box models," CIGRE JWG A2/C4.52, Apr. 2023. [Online]. Available: https://www.cigre.org/GB/publications/e_cigre
- [10] E. Bjerkan and H. K. Høidalen, "High frequency FEM-based power transformer modeling: Investigation of internal stresses due to network-initiated overvoltages," *Electric Power Syst. Res.*, vol. 77, no. 11, pp. 1483–1489, 2007.
- [11] A. D. Podoltsev, K. G. N. B. Abeywickrama, Y. V. Serdyuk, and S. M. Gubanski, "Multiscale computations of parameters of power transformer windings at high frequencies. Part I: Small-scale level," *IEEE Trans. Magn.*, vol. 43, no. 11, pp. 3991–3998, Nov. 2007.
- [12] S. D. Mitchell and J. S. Welsh, "The influence of complex permeability on the broadband frequency response of a power transformer," *IEEE Trans. Power Del.*, vol. 25, no. 2, pp. 803–813, Apr. 2010.
- [13] K. G. N. B. Abeywickrama, T. Daszczynski, Y. V. Serdyuk, and S. M. Gubanski, "Determination of complex permeability of silicon steel for use in high-frequency modeling of power transformers," *IEEE Trans. Magn.*, vol. 44, no. 4, pp. 438–444, Apr. 2008.
- [14] M. M. Shabestary, A. J. Ghanizadeh, G. B. Gharehpetian, and M. Agha-Mirsalim, "Ladder network parameters determination considering nondominant resonances of the transformer winding," *IEEE Trans. Power Del.*, vol. 29, no. 1, pp. 108–117, Feb. 2014.
- [15] A. Miki, T. Hosoya, and K. Okuyama, "A calculation method for impulse voltage distribution and transferred voltage in transformer windings," *IEEE Trans. Power App. Syst.*, vol. PAS-97, no. 3, pp. 930–939, May 1978.
- [16] M. H. Samimi, S. Tenbohlen, A. A. S. Akmal, and H. Mohseni, "Improving the numerical indices proposed for the FRA interpretation by including the phase response," *Int. J. Elect. Power Energy Syst.*, vol. 83, pp. 585–593, 2016.
- [17] H. Tarimoradi and G. B. Gharehpetian, "Novel calculation method of indices to improve classification of transformer winding fault type, location, and extent," *IEEE Trans. Ind. Informat.*, vol. 13, no. 4, pp. 1531–1540, Aug. 2017.
- [18] Y. Shibuya, T. Matsumoto, and T. Teranishi, "Modelling and analysis of transformer winding at high frequencies," in *Proc. Int. Conf. Power Syst. Transients*, 2005, pp. 1–6.
- [19] R. Del et al., Transformer Design Principles. Boca Raton, FL, USA: CRC Press, 2017.
- [20] P. I. Fergestad and T. Henriksen, "Transient oscillations in multiwinding transformers," *IEEE Trans. Power App. Syst.*, vol. PAS-93, no. 2, pp. 500–509, Mar. 1974.
- [21] B. Gustavsen and Á. Portillo, "A damping factor-based white-box transformer model for network studies," *IEEE Trans. Power Del.*, vol. 33, no. 6, pp. 2956–2964, Dec. 2018.
- [22] S. M. H. Hosseini, M. Vakilian, and G. B. Gharehpetian, "Comparison of transformer detailed models for fast and very fast transient studies," *IEEE Trans. Power Del.*, vol. 23, no. 2, pp. 733–741, Apr. 2008.

- [23] D. J. Wilcox, M. Conlon, and W. G. Hurley, "Calculation of self and mutual impedances for coils on ferromagnetic cores," *IEE Proc. A. Phys. Sci., Meas. Instrum., Manage. Educat., Rev.*, vol. 135, no. 7, pp. 470–476, 1988.
- [24] J. E. Kiwitt, A. Huber, and K. Reiß, "Modellierung geblechter Eisenkerne durch homogene anisotrope Kerne für dynamische Magnetfeldberechnungen," *Elect. Eng.*, vol. 81, no. 6, pp. 369–374, 1999.
- [25] T. Luo, M. G. Niasar, and P. Vaessen, "Two-dimensional frequency-dependent resistance and inductance calculation method for magnetic components with round conductors," *IEEE Trans. Magn.*, vol. 60, no. 1, Jan. 2024, Art. no. 8400211.
- [26] E. E. Mombello and G. A. D. Flórez, "An improved high frequency white-box lossy transformer model for the calculation of power systems electromagnetic transients," *Electric Power Syst. Res.*, vol. 190, Jan. 2021, Art. no. 106838.
- [27] M. Popov, "General approach for accurate resonance analysis in transformer windings," *Electric Power Syst. Res.*, vol. 161, pp. 45–51, 2018.
- [28] F. Nasirpour, A. Heidary, M. G. Niasar, A. Lekić, and M. Popov, "High-frequency transformer winding model with adequate protection," *Electric Power Syst. Res.*, vol. 223, Oct. 2023, Art. no. 109637.
- [29] E. Bjerkan, "High frequency modeling of power transformers. stresses and diagnostics," 2005. [Online]. Available: https://www.osti.gov/etdeweb/ biblio/20843756
- [30] F. Nasirpour, M. G. Niasar, and M. Popov, "Magnetic core effects on the high-frequency behavior of transformers," *Int. J. Elect. Power Energy Syst.*, vol. 159, Aug. 2024, Art. no. 110035.
- [31] M. Popov, L. van der Sluis, R. P. P. Smeets, and J. Lopez Roldan, "Analysis of very fast transients in layer-type transformer windings," *IEEE Trans. Power Del.*, vol. 22, no. 1, pp. 238–247, Jan. 2007.
- [32] B. Gustavsen and A. Semlyen, "Rational approximation of frequency domain responses by vector fitting," *IEEE Trans. Power Del.*, vol. 14, no. 3, pp. 1052–1061, Jul. 1999.
- [33] D. Deschrijver, M. Mrozowski, T. Dhaene, and D. De Zutter, "Macro-modeling of multiport systems using a fast implementation of the vector fitting method," *IEEE Microw. Wireless Compon. Lett.*, vol. 18, no. 6, pp. 383–385, Jun. 2008.
- [34] B. Gustavsen, "Fast passivity enforcement for pole-residue models by perturbation of residue matrix eigenvalues," *IEEE Trans. Power Del.*, vol. 23, no. 4, pp. 2278–2285, Oct. 2008.
- [35] B. Gustavsen, "Improving the pole relocating properties of vector fitting," *IEEE Trans. Power Del.*, vol. 21, no. 3, pp. 1587–1592, Jul. 2006.
- [36] A. Semlyen and B. Gustavsen, "A half-size singularity test matrix for fast and reliable passivity assessment of rational models," *IEEE Trans. Power Del.*, vol. 24, no. 1, pp. 345–351, Jan. 2009.
- [37] CIGRE Technical Brochure 904, "High-frequency transformer and reactor models for network studies, part E: Measurements and transformer design details," CIGRE JWG A2/C4.52, Apr. 2023. [Online]. Available: https://www.cigre.org/GB/publications/e_cigre
- [38] Accessed: Jun. 1, 2024. [Online]. Available: www.sintef.no/cigretransformerdata

Farzad Nasirpour received the M.Sc. degree in electrical power systems engineering from the University of Tehran, Tehran, Iran, in 2020. He is currently working toward the Ph.D. degree in electrical power engineering with the Delft University of Technology, Delft, the Netherlands.

Tianming Luo (Member, IEEE) received the M.Sc. degree from China Electric Power Research Institute, Beijing, China, in 2018. He is currently working toward the Ph.D. degree with High Voltage Technologies Group, Delft University of Technology, Delft, the Netherlands.

Mohamad Ghaffarian Niasar (Member, IEEE) received the M.Sc. degree in electrical power engineering from the Sharif University of Technology, Tehran, Iran, in 2008, and the Ph.D. degree in electrical engineering from the KTH Royal Institute of Technology, Stockholm, Sweden, in 2015. He is currently an Assistant Professor with High Voltage Technology Group, Technical University of Delft, Delft, the Netherlands.

Marjan Popov (Member, IEEE) received the Ph.D. degree in electrical power engineering from the Delft University of Technology, Delft, the Netherlands, in 2002. He is currently a Professor of power system protection with the Delft University of Technology and the Director with the Power System Protection Centre.